Appendix from Gutermuth et al., 2009, ApJS, 184, 18

California Institute of Technology, funded by the National Aeronautics and Space Administration and the National Science Foundation. This research has made use of the SIMBAD database, operated at CDS, Strasbourg, France. This work is based in part on observations made with the Spitzer Space Telescope, which is operated by the Jet Propulsion Laboratory, California Institute of Technology under a contract 1407 with NASA. Support for the IRAC instrument was provided by NASA through contract 960541 issued by JPL.

Facilities: Spitzer.

APPENDIX A

UPDATING THE GUTERMUTH ET AL. (2008B) CLASSIFICATION SCHEME

We have used a slightly modified version of the Gutermuth et al. (2008b) multiphase source classification scheme to classify all sources detected in the survey. For the convenience of the reader, we present the scheme here and note the changes made over the original method.

A.1. Phase 1: IRAC Four-band Source Characterization

We apply Phase 1 to all sources that have photometric uncertainties $\sigma < 0.2$ mag detections in all four IRAC bands. We begin by separating out IR-excess contaminants such as star-forming galaxies and broad-line AGNs and then isolate YSOs with IR-excess from those without and finally split the Class I from the more prominent Class II YSOs.

In order to obtain a clean sample of confident YSOs, several contaminating source types can be isolated and removed by application of constraints in various color spaces where these sources are considerably more prominent than YSOs.

First, we eliminate the active star-forming galaxies, as their strong PAH-feature emission yields very red 5.8 and 8.0 μm colors (Stern et al. 2005). We utilize customized cuts in the [4.5] − [5.8] versus [5.8] − [8.0] and [3.6] − [5.8] versus [4.5] − [8.0] color–color spaces to identify and remove these contaminants from our sample.

Any sources are considered PAH galaxies if they follow all of the following constraints:

$$[4.5] - [5.8] < \frac{1.05}{1.2} \times ([5.8] - [8.0] - 1)$$

$$[4.5] - [5.8] < 1.05$$

$$[5.8] - [8.0] > 1$$

$$[4.5] > 11.5.$$

In addition, we also consider sources that obey all of the following constraints to be PAH galaxies:

$$[3.6] - [5.8] < \frac{1.5}{2} \times ([4.5] - [8.0] - 1)$$

$$[3.6] - [5.8] < 1.5$$

$$[4.5] - [8.0] > 1$$

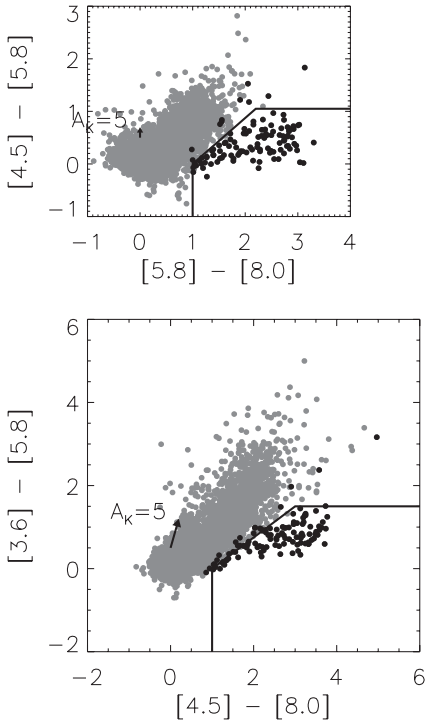

Figure 13. Color–color diagrams used for the isolation of unresolved star-forming galaxies (filled black circles).

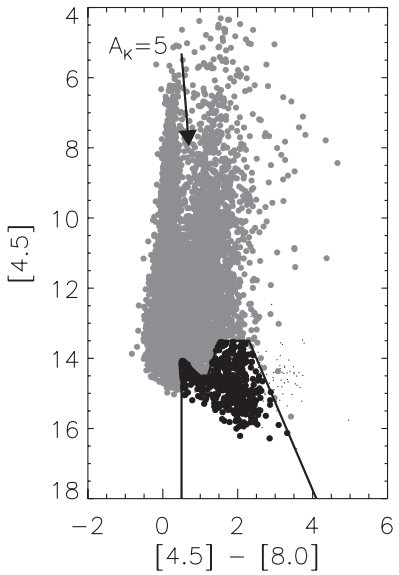

Figure 14. Color–magnitude diagram used for the isolation of broad-line AGNs (filled black circles) from other unclassified sources (filled gray circles). Previously classified sources are excluded (small black dots).

$$[4.5] > 11.5.$$

See Figure 13 for displays of these constraints applied to the data. Once a source has been flagged as a PAH galaxy, it is removed from further consideration in the classification scheme. Since these objects have distnct color differences relative to YSOs, we expect there to be negligible residual contamination from these objects in our YSO lists.

Broad-line AGN have mid-IR colors that are largely consistent with YSOs (Stern et al. 2005). We utilize the [4.5] versus [4.5] − [8.0] color–magnitude diagram (Figure 14) to flag as

likely AGN all sources that follow all of these three conditions:

$$[4.5] - [8.0] > 0.5$$

$$[4.5] > 13.5 + ([4.5] - [8.0] - 2.3)/0.4$$

$$[4.5] > 13.5.$$

Additionally, a source flagged as a likely AGN must follow any one of the following three conditions:

$$[4.5] > 14 + ([4.5] - [8.0] - 0.5)$$

$$[4.5] > 14.5 - ([4.5] - [8.0] - 1.2)/0.3$$

$$[4.5] > 14.5.$$

See Figure 14 for displays of these constraints applied to the data. Even with these cuts applied, a small number of AGN per square degree are expected to be brighter than the magnitude-based cutoff, resulting in contamination of our YSO list. Gutermuth et al. (2008b) reduced ~7.7 deg^2 of the Bootes Shallow Survey field with the Cluster Grinder data treatment in order to estimate the residual contamination of the mitigation and YSO classification effort presented there. With the updated scheme presented here, we have improved on the residual contamination estimates presented there. The reclassified Bootes field data yields a mean expected contamination of 4.8 ± 0.8 class I YSOs and 3.1 ± 0.6 class II YSOs per square degree, for a total contamination of 7.9 ± 1.0 YSOs per square degree.

Unresolved knots of shock emission are often detected in all IRAC bands, yielding yet another source of contamination in our YSO samples. Based on our findings, all sources with photometry that obeys all of the following constraints are likely dominated by shock emission and thus are removed:

$$[3.6] - [4.5] > \frac{1.2}{0.55} \times (([4.5] - [5.8]) - 0.3) + 0.8$$

$$[4.5] - [5.8] \leqslant 0.85$$

$$[3.6] - [4.5] > 1.05.$$

See Figure 15 for a display of these constraints applied to the data. An additional set of contaminant sources are those where resolved structured PAH emission has contaminated the photometric apertures of some dim field stars, leading to spurious excess emission in the 5.8 and 8.0 μm bandpasses. All sources that obey all of the following constraints are consistent with sources that have PAH-contaminated apertures:

$$\sigma_1 = \sigma\{[[4.5] - [5.8]]\}$$

$$\sigma_2 = \sigma\{[[3.6] - [4.5]]\}$$

$$[3.6] - [4.5] - \sigma_2 \leqslant 1.4 \times (([4.5] - [5.8]) + \sigma_1 - 0.7) + 0.15$$

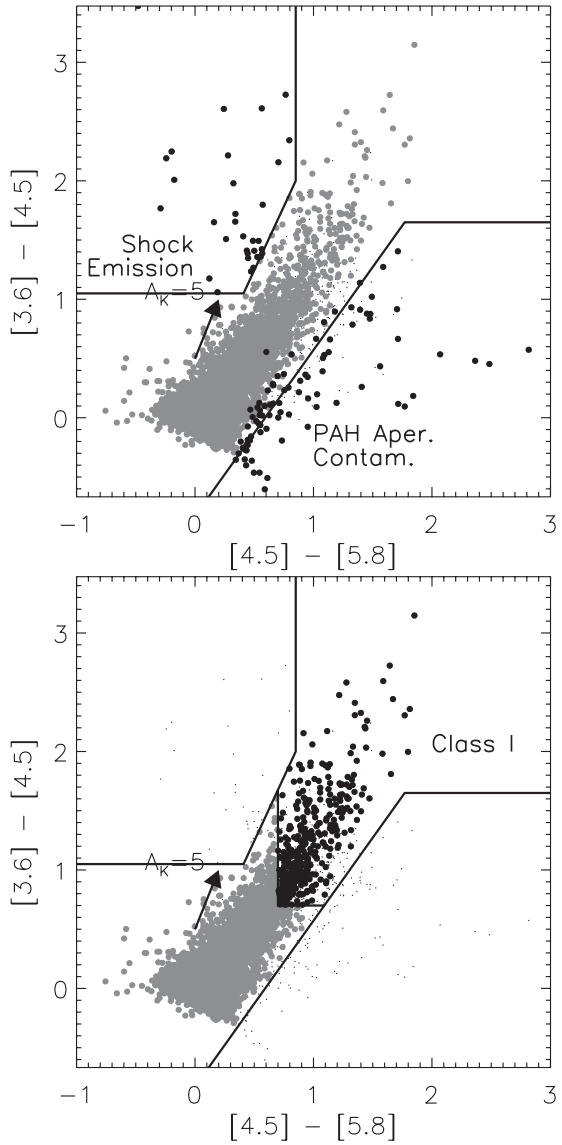

Figure 15. Color–color diagram used for the isolation of unresolved shock emission knots, objects that suffer from structured PAH aperture contamination (filled black circles in top plot), and finally Class I YSOs (filled black circles in bottom plot) from previously unclassified sources (filled gray circles). Previously classified sources are excluded (small black dots).

$$[3.6] - [4.5] - \sigma_2 \leqslant 1.65.$$

See Figure 15 for a display of these constraints applied to the data.

Of the sources that remain, we identify those that obey the following constraints as Class I YSOs, due to their particularly red discriminant colors:

$$\sigma_3 = \sigma[4.5] - [5.8] > 0.7$$

$$\sigma_4 = \sigma[3.6] - [4.5] > 0.7.$$

See Figure 15 for a display of these constraints applied to the data. Note that this is a somewhat simplified version of the protostar criteria of Gutermuth et al. (2008b). It is worth noting that in rare cases, a highly reddened Class II source could have the colors of a Class I as defined above. For those objects with

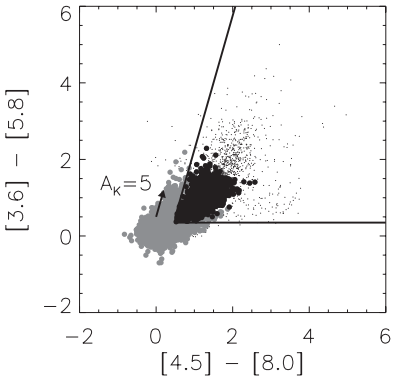

Figure 16. Color–color diagram used for the isolation of Class II YSOs (filled black circles) from previously unclassified sources (filled gray circles). Previously classified sources are excluded (small black dots).

24 μm detections, we can extract these interlopers and reclassify them (see Section A.3 below).

With those objects extracted, we finally can extract the Class II YSOs from the remaining field stars by identifying those sources that follow these constraints:

$$[4.5] - [8.0] - \sigma_3 > 0.5$$

$$[3.6] - [5.8] - \sigma_4 > 0.35$$

$$[3.6] - [5.8] + \sigma_4 \leqslant \frac{0.14}{0.04} \times (([4.5] - [8.0] - \sigma_3) - 0.5) + 0.5$$

$$[3.6] - [4.5] - \sigma_4 > 0.15.$$

See Figure 16 for a display of these constraints applied to the data.

A.2. Phase 2: Additional YSOs Identified via a JHK$_S$[3.6][4.5] YSO Classification Scheme

We apply Phase 2 to those sources that lack detections at either 5.8 or 8.0 μm, but have high quality ($\sigma < 0.1$ mag) 2MASS near-infrared detections in bands (H and K_S are required at minimum, J is used where present) sufficient to enable distinction between sources with IR-excess and those that are simply reddened by dust along the line of sight (Gutermuth 2005).

First we measure the line of sight extinction to each source as parameterized by the E_{H-K} color excess from line of sight extinction from dust. For objects where we have J photometry in addition to H and K_S, we utilize the $\frac{E_{J-H}}{E_{H-K}}$ color excess ratio with baseline colors based on the Classical T Tauri Star (CTTS) locus of Meyer et al. (1997) and standard dwarf star colors (Bessell & Brett 1988). To accomplish the latter, we force $[J-H]_0 \geqslant 0.6$, a simplifying approximation for the intrinsic colors of low mass dwarfs.

Here are the equations used to derive the adopted intrinsic colors from the photometry we have measured (see left panel of Figure 17):

$$[J-H]_0 = 0.58 \times [H-K]_0 + 0.52; \text{ for } [H-K]_0 > 0.14$$

$$[J-H]_0 = 0.6; \text{ for } [H-K]_0 \leqslant 0.14$$

$$[H-K]_0 = [H-K]_{\rm meas} - ([J-H]_{\rm meas} - [J-H]_0) \times \frac{E_{H-K}}{E_{J-H}}$$

$$[H-K]_0 = \frac{[J-H]_{\rm meas} - \frac{E_{J-H}}{E_{H-K}} \times [H-K]_{\rm meas} - 0.52}{0.58 - \frac{E_{J-H}}{E_{H-K}}}$$

For objects that lack J photometry, we use the $\frac{E_{[3.6]-[4.5]}}{E_{H-K}}$ color excess ratio derived from the color excess ratios reported in Flaherty et al. (2007), with baseline colors based on the $H-K$ versus [3.6] − [4.5] color–color space YSO locus, as measured by Gutermuth (2005), and standard dwarf star colors (Bessell & Brett 1988). To accomplish the latter, we force $[H-K]_0 \geqslant 0.2$, a simplifying approximation for the intrinsic colors of low mass dwarfs (see right panel of Figure 17):

$$\begin{aligned}[H-K]_0 &= 1.33 \times [[3.6]-[4.5]]_0 \\ &\quad +0.133; \quad \text{for } [[3.6]-[4.5]]_0 > 0.06\end{aligned}$$

$$[H-K]_0 = 0.2; \text{ for } [[3.6]-[4.5]]_0 \leqslant 0.06$$

$$C = \frac{E_{[3.6]-[4.5]}}{E_{H-K}}$$

$$\begin{aligned}[H-K]_0 &= [H-K]_{\rm meas} - \frac{1}{C}([[3.6]-[4.5]]_{\rm meas} \\ &\quad -[[3.6]-[4.5]]_0)\end{aligned}$$

$$[H-K]_0 = \frac{1.33 \times (C[H-K]_{\rm meas} - [[3.6]-[4.5]]_{\rm meas}) - 0.133}{1.33C - 1}.$$

Once we have measured the component of the $H-K$ color excess that is caused by reddening, we compute the dereddened $K-[3.6]$ and [3.6] − [4.5] colors using the color excess ratios presented in Flaherty et al. (2007), specifically $\frac{E_{J-H}}{E_{H-K}} = 1.73$, $\frac{E_{H-K}}{E_{K-[3.6]}} = 1.49$, and $\frac{E_{H-K}}{E_{K-[4.5]}} = 1.17$:

$$\begin{aligned}[K-[3.6]]_0 &= [K-[3.6]]_{\rm meas} - ([H-K]_{\rm meas} \\ &\quad - [H-K]_0) \times \frac{E_{K-[3.6]}}{E_{H-K}}\end{aligned}$$

$$\begin{aligned}[[3.6]-[4.5]]_0 &= [[3.6]-[4.5]]_{\rm meas} - ([H-K]_{\rm meas} \\ &\quad - [H-K]_0) \times \frac{E_{[3.6]-[4.5]}}{E_{H-K}}\end{aligned}$$

$$\frac{E_{[3.6]-[4.5]}}{E_{H-K}} = \left\{ \left[\frac{E_{H-K}}{E_{K-[4.5]}} \right]^{-1} - \left[\frac{E_{H-K}}{E_{K-[3.6]}} \right]^{-1} \right\}^{-1}.$$

We now identify additional YSOs as those sources with dereddened colors that obey all of the following constraints (see Figure 18):

$$\sigma_1 = \sigma\{[[3.6]-[4.5]]_{\rm meas}\}; \sigma_2 = \sigma\{[[K]-[3.6]]_{\rm meas}\}$$

$$[[3.6]-[4.5]]_0 - \sigma_1 > 0.101$$

$$[K-[3.6]]_0 - \sigma_2 > 0$$

$$\begin{aligned}[K-[3.6]]_0 - \sigma_2 &> -2.85714 \times ([[3.6] \\ &\quad -[4.5]]_0 - \sigma_1 - 0.101) + 0.5.\end{aligned}$$

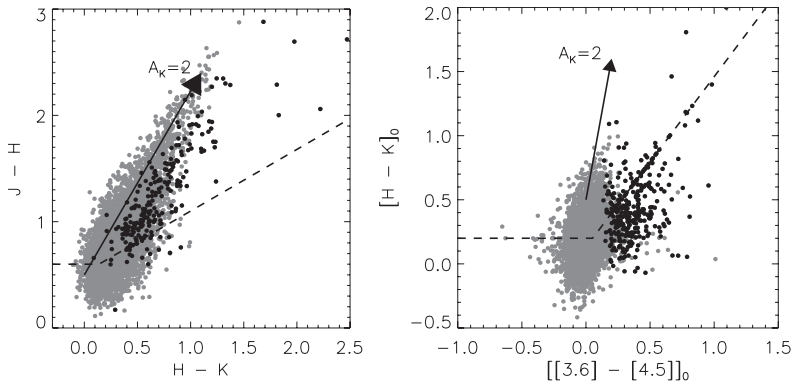

Figure 17. Color–color diagrams used for measuring extinction for subsequent dereddening efforts. YSOs isolated by the Phase 2 classification (see Section A.2 and Figure 18) are plotted as filled black circles. The reference loci adopted for the extinction measurements are plotted as dashed black lines.

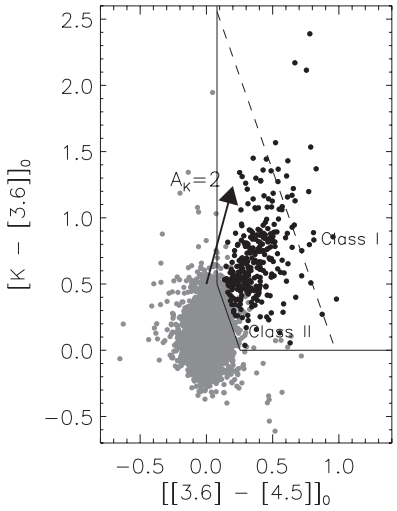

Figure 18. Color–color diagram used for isolation of Class I and Class II YSOs (filled black circles) in the Phase 2 classification. The dashed black line denotes the separation between the Class I and Class II YSOs.

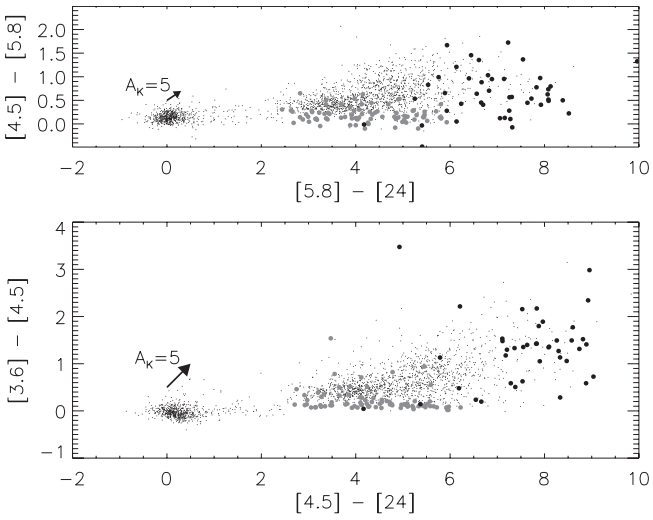

Figure 19. Color–color diagrams used for the isolation of transition disk objects (filled gray circles) and deeply embedded protostars (filled black circles).

Among these YSOs, sources that also follow the following selection are considered likely protostars, the rest are considered Class II:

$$[K - [3.6]]_0 - \sigma_2 > -2.85714 \times ([[3.6] - [4.5]]_0 - \sigma_1 - 0.401) + 1.7.$$

To minimize the inclusion of dim extragalactic contaminants, we apply a simple brightness limit using the dereddened 3.6 μm photometry. All sources classified as Class II with this method must have $[3.6]_0 < 14.5$ and all protostars must have $[3.6]_0 < 15$.

A.3. Phase 3: Adding and Checking YSOs with MIPS 24 μm Photometry

We apply Phase 3 to all objects with MIPS 24 μm detections with $\sigma < 0.2$ mag. Phase 3 is primarily a MIPS 24 μm reexamination of the entire catalog, including transition disk sources (Class III sources as classified by shorter wavelengths, but with large 24 μm excess) and deeply embedded YSOs with insufficient IRAC and 2MASS bandpass coverage to have been included by the previous two phases but with bright ([24] < 7) MIPS detections. Phase 3 also includes a search for heavily reddened Class II sources that were misclassified as Class I in Phase 1, identified by a lack of adequate 24 μm excess.

First, sources that were considered photospheric in the previous two phases but have excess emission at 24 μm ($[5.8] - [24] > 2.5$ or $[4.5] - [24] > 2.5$) are very interesting (filled gray circles in Figure 19). These sources are typically "Transition Disks," Class II sources with significant dust clearing within their inner disks. We have required that valid sources in this group also have $[3.6] < 14$ in an effort to minimize contamination from extragalactic contaminants. These objects are marked as class "II" with an asterisk to note their special nature in the tables.

Second, many young sources are so deeply embedded that we cannot extract usable photometry in one or more of the four IRAC bands. As such, we note any source as a likely deeply embedded protostar[7] if it lacks detections in some IRAC bands yet has bright MIPS 24 μm photometry ([24] < 7 and $[X] - [24] > 4.5$ mag, where $[X]$ is the photometry for the longest wavelength IRAC detection that we possess). The adopted magnitude limit at 24 μm is needed to mitigate extragalactic source contamination. The specific value that we adopt here is slightly more conservative than that adopted by c2d (Harvey et al. 2006). Furthermore, with the addition of the 24 μm data, we have more information to filter lower

[7] Classifying sources as bona fide Class 0 protostars requires a detailed treatment including submillimeter flux measurements which are beyond the scope of this paper. As such, these sources are still labeled Class I in Table 5, but with the addition of an asterisk to note their anomalous nature.

luminosity YSOs from our AGN candidates and shock emission dominated sources flagged in Section A.1. We reinclude flagged sources as likely protostars if they have both bright MIPS 24 μm photometry ([24] < 7, as before) and convincingly red IRAC/MIPS colors ([3.6] $-$ [5.8] > 0.5 and [4.5] $-$ [24] > 4.5 and [8.0] $-$ [24] > 4). The filled black circles in Figure 19 show the full distribution of these objects in the IRAC and MIPS 24 μm color planes.

Finally, all previously identified protostars that have 24 μm detections are checked to ensure that their SEDs do indeed continue to rise from IRAC to MIPS wavelengths. All protostars that have MIPS detections must have [5.8] $-$ [24] > 4 if they possess 5.8 μm photometry, otherwise they must have [4.5]$-$[24] > 4. If a source does not meet this color requirement, it is likely a highly reddened Class II and reclassified as such.

APPENDIX B

CIRCLES, ELLIPSES, CONVEX HULLS, AND ASPECT RATIOS

The choice of method for determining the circular radius of a source grouping, $R_{\rm circ}$, is an important one, as not only is this an overall cluster size measurement, it is also a key component of the measurement of aspect ratios of non-circular distributions. In the case of an approximately elliptical distribution, $R_{\rm circ}$ is the semimajor axis of the elliptical area. As mentioned in Section 5, we have departed from the more standard definition of the circular radius of a cluster (the radial distance from the mean of the source positions to the furthest source; e.g., Cartwright & Whitworth 2004). Instead, we chose to use the radial distance to the most distant source from use the mean position of those sources that are the vertices of the convex hull. This method is much less susceptible to bias from the high uncertainty of the mean position of small-N groupings, and is therefore less likely to overestimate the cluster area, such as was illustrated by Schmeja & Klessen (2006) for the standard circular radius definition. Note that for large-N uniform or centrally concentrated groupings, the two methods produce nearly identical results.

Schmeja & Klessen (2006) defined the "elongation" of a cluster, ξ, as $R_{\rm circ}/R_{\rm hull}$ and then performed numerous Monte Carlo realizations of uniform surface density $N = 350$ member clusters distributed in elliptical areas of varying aspect ratio to demonstrate the efficacy of ξ as a functional tracer of the aspect ratio of the elliptical area. This result can be demonstrated trivially in analytic form if we assume N is sufficiently large (350 is large), as the resulting convex hull of an elliptical distribution of sources can be approximated by a true ellipse. The assumption of large N also ensures that the mean position of sources has very low uncertainty, that statistical non-uniformity in the overall source distribution is kept to a relatively low level, and that the convex hull area adjustment for the fraction of sources making up the vertices of the hull is approximately unity. As such, the area of the convex hull is πab, where a and b are the semimajor and semiminor axes of the ellipse, respectively. It follows then that $R_{\rm hull} = \sqrt{(ab)}$ given its definition in Section 5. As mentioned above, $R_{\rm circ}$ in this case is just the semimajor axis, a, and thus the 'elongation' is simply $\sqrt{(a/b)}$, the square root of the aspect ratio of the ellipse, a result that is born out in the Monte Carlo simulations of Schmeja & Klessen (2006). For conceptual simplicity, we have chosen to ignore the "elongation" value, ξ, and instead report its square, the elliptical equivalent aspect ratio.

As can be noted in Tables 7 and 8, there are several regions with reported aspect ratios below 1, contrary to the definition of that quantity. These typically arise in small-N groups that are effectively circular, but the granularity of the convex hull area adjustment for small-N groups results in relatively high uncertainty in the measured value of $R_{\rm hull}$. It is important to note the uncertainty in the convex hull area associated with placing one object more or less on the convex hull increases rapidly as N decreases and as the fraction of members that are convex hull vertices increases.

REFERENCES

Adams, F. C., Proszkow, E. M., Fatuzzo, M., & Myers, P. C. 2006, ApJ, 641, 504
Allen, L., et al. 2007, in Protostars and Planets V, ed. B. Reipurth, D. Jewitt, & K. Keil (Tucson, AZ: Univ. of Arizona Press), 361
Allen, L. E., et al. 2004, ApJS, 154, 363
Allen, L. E., Myers, P. C., Di Francesco, J., Mathieu, R., Chen, H., & Young, E. 2002, ApJ, 566, 993
Allen, T. S., et al. 2008, ApJ, 675, 491
Allen, T. S., et al. 2009, ApJ, submitted
Ballesteros-Paredes, J., Klessen, R. S., Mac Low, M.-M., & Vazquez-Semadeni, E. 2007, in Protostars and Planets V, ed. B. Reipurth, D. Jewitt, & K. Keil (Tucson, AZ: Univ. of Arizona Press), 63
Baraffe, I., Chabrier, G., Allard, F., & Hauschildt, P. H. 1998, A&A, 337, 403
Bastian, N., Ercolano, B., Gieles, M., Rosolowsky, E., Scheepmaker, R. A., Gutermuth, R., & Efremov, Y. 2007, MNRAS, 379, 1302
Bastian, N., Gieles, M., Ercolano, B., & Gutermuth, R. 2009, MNRAS, 392, 868
Bate, M. R., Bonnell, I. A., & Bromm, V. 2003, MNRAS, 339, 577
Battinelli, P. 1991, A&A, 244, 69
Bessell, M. S., & Brett, J. M. 1988, PASP, 100, 1134
Blaauw, A. 1964, ARA&A, 2, 213
Bonnell, I. A., Bate, M. R., & Vine, S. G. 2003, MNRAS, 343, 413
Carpenter, J. M. 2000, AJ, 120, 3139
Cartwright, A., & Whitworth, A. P. 2004, MNRAS, 348, 589
Casertano, S., & Hut, P. 1985, ApJ, 298, 80
Chavarria, L., Allen, L., Hora, J. L., Brunt, C., & Fazio, G. G. 2009, ApJ, 682, 445
Comerón, F. 2008, in the Handbook of Low Mass Star Formation in Southern Molecular Clouds, Vol II, ed. B. Reipurth (San Francisco, CA: ASP Monograph), 295
Crapsi, A., van Dishoeck, E. F., Hogerheijde, M. R., Pontoppidan, K. M., & Dullemond, C. P. 2008, A&A, 486, 245
de Zeeuw, P. T., Hoogerwerf, R., de Bruijne, J. H. J., Brown, A. G. A., & Blaauw, A. 1999, AJ, 117, 354
Fazio, G. G., et al. 2004, ApJS, 154, 10
Flaherty, K. M., Pipher, J. L., Megeath, S. T., Winston, E. M., Gutermuth, R. A., Muzerolle, J., Allen, L. E., & Fazio, G. G. 2007, ApJ, 663, 1069
Fűrész, G., Hartmann, L. W., Megeath, S. T., Szentgyorgyi, A. H., & Hamden, E. T. 2008, ApJ, 676, 1109
Gammie, C. F., Lin, Y.-T., Stone, J. M., & Ostriker, E. C. 2003, ApJ, 592, 203
Getman, K. V., Feigelson, E. D., Townsley, L., Broos, P., Garmire, G., & Tsujimoto, M. 2006, ApJS, 163, 306
Gomez, M., Hartmann, L., Kenyon, S. J., & Hewett, R. 1993, AJ, 105, 1927
Gutermuth, R. A., Megeath, S. T., Pipher, J. L., Williams, J. P., Allen, L. E., Myers, P. C., & Raines, S. N. 2005, ApJ, 632, 397
Gutermuth, R. A. 2005, PhD thesis Univ. of Rochester
Gutermuth, R. A., et al. 2008a, ApJ, 673, L151
Gutermuth, R. A., et al. 2008b, ApJ, 674, 336
Haisch, K. E., Jr., Lada, E. A., & Lada, C. J. 2001, ApJ, 553, L153
Harvey, P. M., et al. 2006, ApJ, 644, 307
Harvey, P., Merín, B., Huard, T. L., Rebull, L. M., Chapman, N., Evans, N. J., II, & Myers, P. C. 2007, ApJ, 663, 1149
Harvey, P. M., et al. 2008, ApJ, 680, 495
Hatchell, J., Fuller, G. A., Richer, J. S., Harries, T. J., & Ladd, E. F. 2007, A&A, 468, 1009
Herbig, G. H., Andrews, S. M., & Dahm, S. E. 2004, AJ, 128, 1233
Hernández, J., et al. 2007, ApJ, 662, 1067
Hillenbrand, L. A., Bauermeister, A., & White, R. J. 2008, in ASP Conf. Ser. 384, 14th Cambridge Workshop on Cool Stars, Stellar Systems, and the Sun, ed. G. van Belle (San Francisco, CA: ASP), 200
Hillenbrand, L. A., Meyer, M. R., Strom, S. E., & Skrutskie, M. F. 1995, AJ, 109, 280